

# Saturn's G ring: insights from the dynamical evolution of dust particles from the G-ring arc

Zhengan Chen,<sup>1,2</sup> Xiaodong Liu,<sup>1,2</sup> and Kun Yang<sup>1,2\*</sup>

<sup>1</sup>*School of Aeronautics and Astronautics, Shenzhen Campus of Sun Yat-sen University, Shenzhen, Guangdong 518107, China*

<sup>2</sup>*Shenzhen Key Laboratory of Intelligent Microsatellite Constellation, Shenzhen Campus of Sun Yat-sen University, Shenzhen, Guangdong 518107, China*

Accepted XXX. Received YYY; in original form ZZZ

## ABSTRACT

To explore the formation and properties of Saturn's G ring, we study the dynamics of micron-sized dust particles originating from the arc of debris near the inner edge of the ring. The dynamical evolution of particles due to various perturbation forces and the plasma sputtering that erodes the particles is simulated by a well-tested numerical code. Based on the simulation results, the normal  $I/F$  of the G ring observed by the Cassini spacecraft can be explained by dust particles originating from the arc. Other properties of the G ring are also estimated, including the steady-state size distribution and the number density of ring particles, the geometric optical depth, the apparent edge-on thickness, the age and the remaining lifetime of the G ring. We find that the particle size distribution of the G ring follows a power law with an exponent of 2.8, and dust particles in the size range of  $[5, 10] \mu\text{m}$  are dominant within the ring. The average number density of particles of the G ring in the radial direction is about  $10^{-3}\text{--}10^{-2} \text{ m}^{-3}$ . The peak value of the edge-on geometric optical depth of the G ring is about  $3.9 \times 10^{-2}$ . The maximum apparent edge-on thickness of the G ring with the geometric optical depth larger than  $1 \times 10^{-8}$  is approximately 9,000 km. The age of the G ring is estimated to be  $10^6\text{--}10^7$  years, and the remaining lifetime of the ring is on the order of  $10^4$  years.

**Key words:** celestial mechanics – meteorites, meteors, meteoroids – planets and satellites: rings.

## 1 INTRODUCTION

Saturn's G ring is a faint ring composed of micron-sized dust particles, which is located approximately 166,000 to 175,000 km from Saturn. The ring was first imaged by the Voyager 1 in 1980 (Smith et al. 1981). Subsequently, the investigation of the G ring can be divided into two periods: before and after the arrival of the Cassini spacecraft. In the first epoch, several studies (Van Allen 1983; Showalter & Cuzzi 1993; Canup & Esposito 1997; Meyer-Vernet et al. 1998; Throop & Esposito 1998; Lissauer & French 2000) were focused on the structure and particle properties of the G ring. However, most of these studies were carried out by analyzing the observation data, such as the analyses of the proton absorption signature detected by the Pioneer 11 (Van Allen 1983), images obtained by the Voyager 1 and 2 (Showalter & Cuzzi 1993), dust impact signals (Meyer-Vernet et al. 1998) and images obtained by the Hubble Space Telescope (Lissauer & French 2000). Less attention was paid to the dynamics of dust particles within the ring.

After the arrival of the Cassini spacecraft, a bright arc (hereafter refer as "G-ring arc") and a moonlet Aegaeon that orbits within the arc were discovered near the inner edge of the G ring (Hedman et al. 2007, 2010). Scientists began to take an interest in the dynamics of dust particles in order to explore the relationships among the three components of the G-ring system, namely Aegaeon, the arc, and the ring. Madeira et al. (2018) and Madeira & Giuliatti Winter (2020) investigated the roles of Aegaeon in the production and fate of

particles within the G-ring arc by analyzing the dynamical evolution of particles within the arc. They showed that many particles confined in the arc collide with Aegaeon, and Aegaeon is not the only source of particles within the arc. To investigate the formation of the G ring, Maravilla & Leal-Herrera (2014) used an analytical model to study the dynamics of particles ejected from Aegaeon, and suggested that Aegaeon can supply sub-micron and nanometric dust particles to the G ring. Except for Aegaeon, Hedman et al. (2007) proposed that the G-ring arc contains a population of large debris in the size range from centimeters to meters, which also supply dust particles to the G ring. The study on the dynamics of particles within analogous dynamical systems, i.e. the arcs of Saturn's moons Anthe and Methone, showed that particles can escape from the arc due to the plasma drag (Sun et al. 2017). This mechanism may also result in the ejection of particles from the G-ring arc to the G ring.

In this paper, the dynamics of micron-sized dust particles originating from the G-ring arc is studied by high-accuracy numerical simulations to explore the formation and properties of the G ring. Various perturbation forces and the plasma sputtering are taken into account. The dynamical model is described in Sections. 2, and the numerical simulation strategy is given in Sections. 3. In Section. 4, the orbital evolution, the average dynamical lifetimes and the final fates of particles with different sizes are investigated. Based on the study of the dynamics of dust particles and the observations obtained by the Cassini spacecraft, the normal  $I/F$ , the particle properties, the edge-on geometric optical depth, the apparent edge-on thickness, the age and the remaining lifetime of the G ring are estimated and

\* E-mail: yangk77@mail.sysu.edu.cn

analyzed in Section. 5. Finally, the conclusion of this paper is given in Section. 6.

## 2 DYNAMICAL MODEL

Micron-sized dust particles can be generated through the mutual collision between the large debris within the G-ring arc or by the impact of micrometeoroids onto these large bodies. After dust particles start their lives, they are subjected to various perturbation forces, including the effect of planetary oblateness, solar radiation pressure, Poynting-Roberson drag, Lorentz force, plasma drag and the gravity of moons. The equation of dust grain's motion in the equatorial inertial frame of Saturn (SIF), where the  $x$ -axis of SIF points toward the ascending node of Saturn's orbit at J2000, the  $z$ -axis is along the spin axis of Saturn, and the  $y$ -axis is determined by the right-hand rule, is expressed as

$$\begin{aligned} \ddot{\vec{r}} = & GM_S \nabla \left\{ \frac{1}{r} \left[ 1 - \sum_{n=1}^{N_S} J_{2n} \left( \frac{R}{r} \right)^{2n} P_{2n}(\cos \theta) \right] \right\} \\ & + \frac{3S_{\text{flux}} Q_{\text{pr}}}{4\rho_g r_g c} \left\{ \left[ 1 - \frac{(\dot{\vec{r}} - \dot{\vec{r}}_{\text{sun}}) \cdot \vec{S}}{c} \right] \vec{S} - \frac{\dot{\vec{r}} - \dot{\vec{r}}_{\text{sun}}}{c} \right\} \\ & + \frac{3\epsilon_0 \Phi}{\rho_g r_g^2} (\vec{V}_{\text{rel}} \times \vec{B}) - \frac{3N_{W^+} m_{W^+} |\vec{V}_{\text{rel}}|}{4\rho_g r_g} \vec{V}_{\text{rel}} \\ & - \sum \left[ \frac{GM_{\text{moons}}}{|\vec{r} - \vec{r}_{\text{moons}}|^3} (\vec{r} - \vec{r}_{\text{moons}}) + \frac{GM_{\text{moons}}}{|\vec{r}_{\text{moons}}|^3} \vec{r}_{\text{moons}} \right], \end{aligned} \quad (1)$$

where  $\vec{r}$  is the radius vector of the grain,  $M_S$  the mass of Saturn,  $R$  the reference radius for gravitational field of Saturn,  $J_{2n}$  and  $P_{2n}$  the Saturn's zonal harmonics and the Legendre functions of degree  $2n$ , and  $\theta$  the colatitude of the grain in the Saturn-centered body-fixed frame. The parameters of Saturn gravity field are taken from Jacobson (2022), where the  $J_2$ ,  $J_4$  and  $J_6$  are considered here, i.e.,  $N_S = 3$ . The variable  $S_{\text{flux}}$  is the solar flux at the distance of Saturn's orbit around the Sun, and  $Q_{\text{pr}}$  is the solar radiation pressure efficiency calculated by Mie theory (Burns et al. 1979). The bulk density of the grain  $\rho_g = 540 \text{ kg m}^{-3}$  is assumed to be consistent with that of Aegaeon, the value of which is taken from Thomas et al. (2013). The variable  $r_g$  is the grain size,  $c$  the speed of light,  $\vec{r}_{\text{sun}}$  the radius vector of the Sun, and  $\vec{S}$  the unit vector from the Sun to the grain.

The variable  $\epsilon_0$  is the vacuum permittivity, and  $\vec{V}_{\text{rel}}$  is the velocity of the grain relative to the corotation velocity which is calculated by  $\vec{V}_{\text{corotate}} = \Omega_S \times \vec{r}$ , where  $\Omega_S$  is the spin rate of Saturn. As suggested by Wahlund et al. (2005), the electric potential  $\Phi$  of the surface of dust grain in the G ring is close to that of the Cassini spacecraft when it orbits above the G ring, where the value is about  $-2 \text{ V}$ . The coefficient of Saturn's magnetic field  $\vec{B}$  is adopted from Dougherty et al. (2018). The plasma distribution in the inner magnetosphere of Saturn derived by Persoon et al. (2020) is used to calculate the plasma drag. The variable  $N_{W^+}$  is the number density of water group ions  $W^+$ . The average mass  $m_{W^+}$  is 17.5 amu, and the velocity of the plasma is assumed to equal the corotation velocity. The variables  $M_{\text{moons}}$  and  $\vec{r}_{\text{moons}}$  are the mass and the radius vector of moons. The gravitational perturbations induced by Mimas, Enceladus, Tethys and Aegaeon are considered.

In addition to the perturbation forces, the plasma sputtering which leads to the erosion of dust particles is also taken into account in the simulations. The relationship between the sputtering yield (and thus the sputtering rate, as shown in Johnson et al. (2008)) and the grain size has been investigated by Jurac et al. (2001), which showed

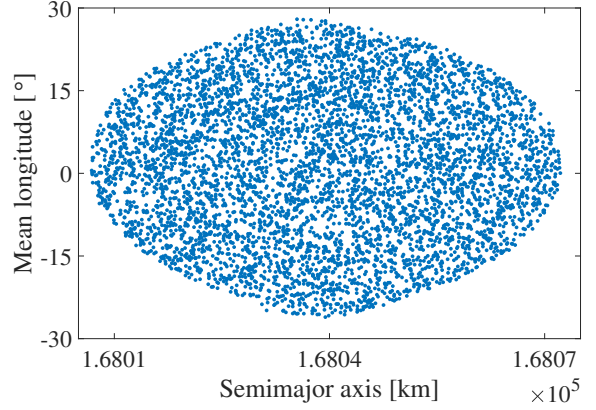


**Figure 1.** Initial semi-major axes and mean longitudes of the simulated particles.

that the sputtering yield is approximately the same for particles with different sizes when the incident ion energy is less than 1 keV. Because the energy of the plasma in the vicinity of the G ring is smaller than 100 eV (Tseng et al. 2013), in our work the sputtering rate is assumed to be the same regardless of the particle's initial size in the simulations. Additionally, since the locations of Saturn's E and G rings are close to each other, the sputtering rate is assumed to be the same as that of the E ring particles in our simulation, which reads (Jurac et al. 2001; Juhász & Horányi 2002)

$$r_g(t_y) = r_{g0} - \frac{t_y}{50} \times 10^{-6}, \quad (2)$$

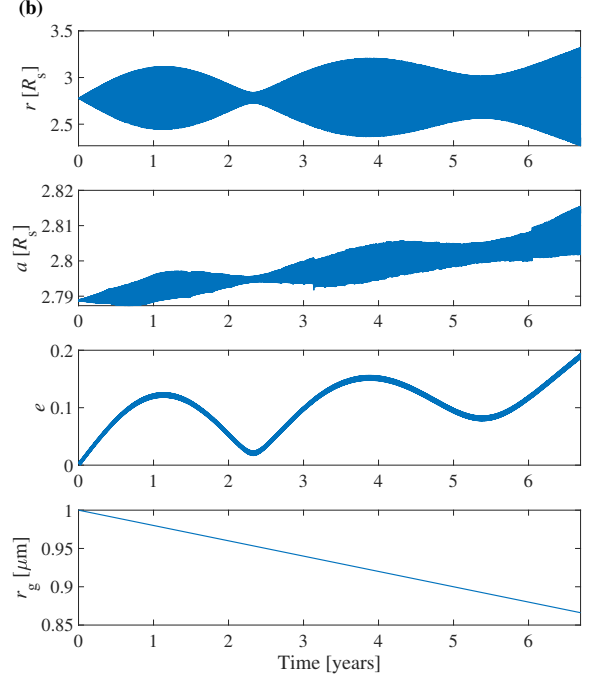
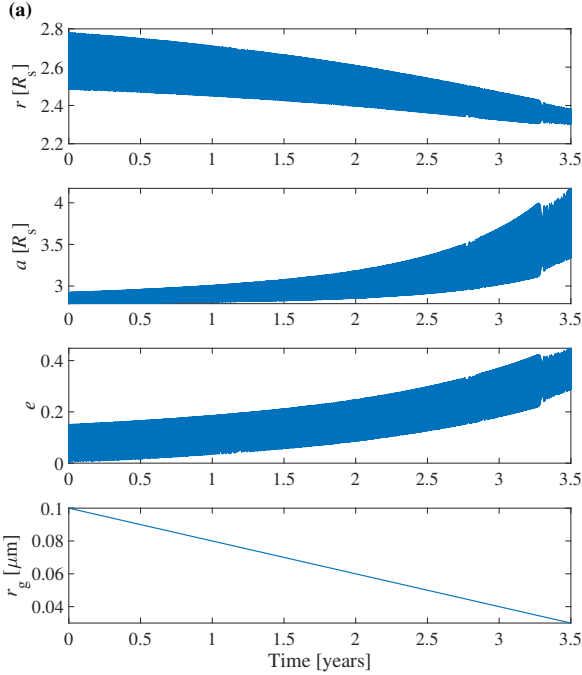
where  $r_{g0}$  is the initial grain radius in meters, and  $t_y$  is the time in years from the moment when the particle is generated from the arc.

By simulating the dynamics of test particles, it is found that dust particles from the G-ring arc spend only a small percent of their lifetimes in Saturn's shadow, and their dynamical evolutions are rarely affected. Therefore, the planetary shadow effects are neglected in simulations of this work.

## 3 NUMERICAL SIMULATION STRATEGY

The G-ring arc and Aegaeon are trapped in a 7:6 corotation eccentricity resonance (CER) with Mimas (Hedman et al. 2007, 2010). The arc is longitudinally confined in  $60^\circ$  and the maximum amplitude of the semimajor axes libration of debris inside the arc is approximately 31 km (Hedman et al. 2007). Meanwhile, Aegaeon stays close to the center of the resonance, where the amplitude of its semimajor axis libration is only a few kilometers (Hedman et al. 2010). As dust particles are generated from the large debris in the arc, the mean longitudes  $\lambda$  of grains are selected to be randomly distributed within  $30^\circ$  from the arc's center, and the semimajor axes  $a$  are selected to be randomly distributed within 31 km from Aegaeon's semimajor axis. In this way, 1000 particles are selected for each grain size, from which we exclude the particles initially outside the resonance (Madeira & Giulianti Winter 2020), and as a result more than 600 grains per size are simulated finally in our simulation. The initial semimajor axes and mean longitudes of the simulated particles are shown in Fig. 1. Other initial orbital elements of dust particles, including eccentricity  $e$ , inclination  $i$ , longitude of ascending node  $\Omega$  and argument of pericenter  $\omega$ , are simply assumed to be the same as those of Aegaeon.

The dynamical evolution of dust grains with 9 different grain sizes,



including  $0.1 \mu\text{m}$ ,  $0.2 \mu\text{m}$ ,  $0.5 \mu\text{m}$ ,  $1 \mu\text{m}$ ,  $2 \mu\text{m}$ ,  $5 \mu\text{m}$ ,  $10 \mu\text{m}$ ,  $20 \mu\text{m}$ , and  $50 \mu\text{m}$ , is simulated by a well-tested code (see Liu et al. 2016; Liu & Schmidt 2018, 2021; Yang et al. 2022; Chen et al. 2024). The simulation stops if the dust grain hits a moon, reaches the outer edge of the A ring ( $\sim 2.27$  equatorial radius of Saturn  $R_S$ ), moves outside the orbital distance of Enceladus ( $\sim 3.95 R_S$ ), or if the grain size decreases to  $0.03 \mu\text{m}$  due to the plasma sputtering.

#### 4 DYNAMICAL EVOLUTION OF DUST PARTICLES

From our simulation results, three typical orbital evolutions of dust particles originating from the G-ring arc are found, as shown in Fig. 2. For dust particles smaller than  $1 \mu\text{m}$ , both of their semimajor axes and eccentricities increase to large values quickly (within a few years) due to the strong effects of perturbation forces, including the Lorentz force, solar radiation pressure and plasma drag. However, their orbital distances from Saturn decrease slowly with time (see Fig. 2a). The grain size of  $1 \mu\text{m}$  seems to be a critical size. For particles with this critical size, their semimajor axes generally increase much slower than that of particles smaller than  $1 \mu\text{m}$ , and their orbital distances oscillate with large amplitudes within a few years due to the large libration of their eccentricities (see Fig. 2b).

For particles larger than  $1 \mu\text{m}$ , their semimajor axes barely change at first since they are trapped in the arc. After a period of time, particles can escape from the arc due to the plasma drag, and their semimajor axes increase slowly with time after leaving the arc. Note that the particle is considered to escape from the arc once its semimajor axis is larger than  $62 \text{ km}$  away from the semimajor axis of Aegaeon. We calculate the average sizes  $r_{\text{escape}}$  of these particles at the moment when they escape from the arc (Fig. 3). Generally, dust particles leave the arc with their grain sizes less than about  $16 \mu\text{m}$ . The eccentricities of these particles remain small during most of their dynamical lifetime, and increase rapidly in the rest of their lifetime due to the strong effects of the Lorentz force and solar radiation pressure. The orbital distances of these particles remain almost constant

during the period when the eccentricities remain small and oscillate significantly in the rest of their lifetime due to the rapid growth of the eccentricities (see Fig. 2c).

The conserved integral of dust particles' motion derived by Hamilton & Krivov (1996) is used to calculate the variation in the maximum value of the eccentricity  $e_{\text{max}}$  of a particle with initial size of  $10 \mu\text{m}$  as its grain size decreases (see Fig. 4). The value of  $e_{\text{max}}$  remains small in the grain size of  $[2, 10] \mu\text{m}$ . After the grain size is smaller than  $2 \mu\text{m}$ , the value of  $e_{\text{max}}$  increases quickly as the grain size decreases. This analytical solution matches well with our numerical results. Note that the value of  $e_{\text{max}}$  calculated by the conserved integral may not be exact when the particle is smaller than  $2 \mu\text{m}$  since the orbit-average approximation for deriving the integral breaks down in this size range. However, the basic variation trend of  $e_{\text{max}}$  is still reliable (Hamilton & Krivov 1996).

Based on the results of the dynamical evolution of dust particles, we analyze the average dynamical lifetimes  $T_{\text{life}}$ , the average times  $T_{\text{arc}}$  that dust particles spend in the arc, and the final fates of particles with different sizes (see Fig. 5 and Table. 1). Note that  $T_{\text{arc}}$  is defined to be the duration from the production moment of particle to the escaping moment of particle from the arc. The  $T_{\text{arc}}$  of dust particles smaller than  $1 \mu\text{m}$  are less than one year, and the  $T_{\text{life}}$  of these particles are determined by the sputtering rate as they are finally removed by the plasma sputtering. Most of  $1 \mu\text{m}$  particles collide with the A ring in a few years due to their orbital distances oscillating with large amplitude. For particles larger than  $1 \mu\text{m}$ , the  $T_{\text{arc}}$  increases with the initial grain size since the decrease in grain size due to the plasma sputtering before the particles leave the arc is proportional to the initial grain size (note that the sputtering rate is the same for particles regardless of their sizes). The dynamical lifetimes of particles after they leave the arc are mainly determined by the time span when the eccentricities of particles remain small (see Fig. 2c), and also increase with the initial grain size. By adding up the dynamical lifetime of particles before and after leaving the arc, the  $T_{\text{life}}$  also increase with the initial grain size.

As seen from Table. 1, most of dust particles with  $r_g > 1 \mu\text{m}$

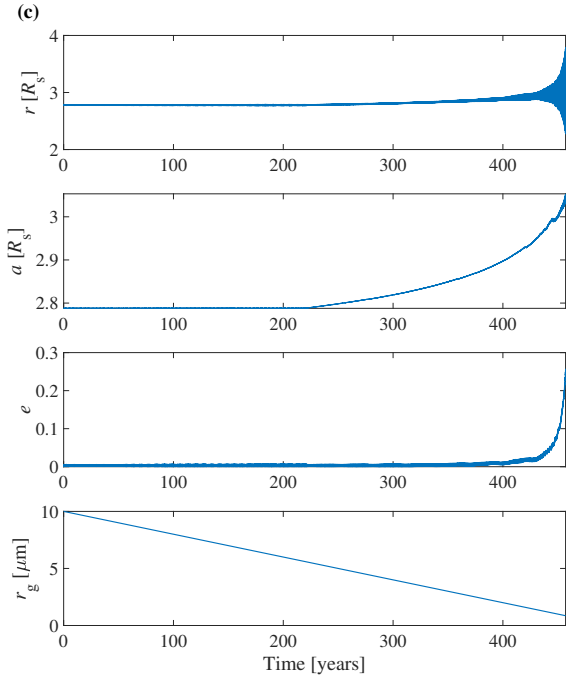


**Figure 2.** *Panel a:* typical orbital evolution, including the orbital distance, semimajor axis and eccentricity, and physical radius evolution of particle with grain size  $r_g < 1 \mu\text{m}$ . *Panel b:* same as *Panel a*, but with grain size  $r_g = 1 \mu\text{m}$ . *Panel c:* same as *Panel a*, but with grain size  $r_g > 1 \mu\text{m}$ .

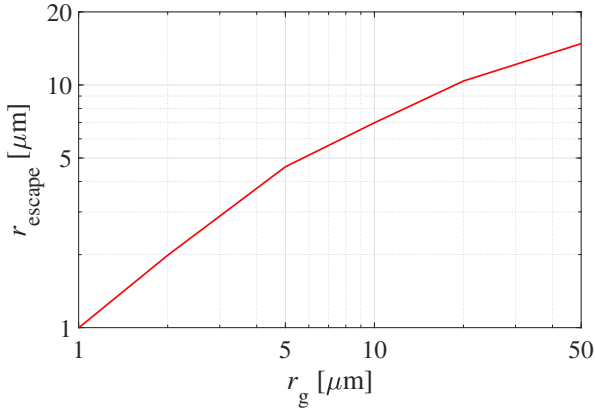


**Figure 3.** Average grain sizes when dust particles escape from the arc as a function of the initial grain size.

collide with the A ring due to the close proximity between the orbital distance of the outer edge of the A ring ( $\sim 2.27 R_s$ ) and the initial orbital distances of particles ( $\sim 2.75 R_s$ ) and the significant oscillation of the orbital distances of particles. However, a fraction of large particles ( $r_g \geq 10 \mu\text{m}$ ) can also migrate outside the orbit of Enceladus ( $\sim 3.95 R_s$ ) due to their long dynamical lifetimes after they leave the arc, which allows their semimajor axes (approximately equal to their orbital distances when the eccentricities are small) to increase to that of Enceladus before their orbital distances oscillating significantly. During the migration, a fraction of particles hit Mimas ( $\sim 3.09 R_s$ ). As large particles move outward slower than small particles and have a larger probability of hitting Mimas, the fraction of particles that

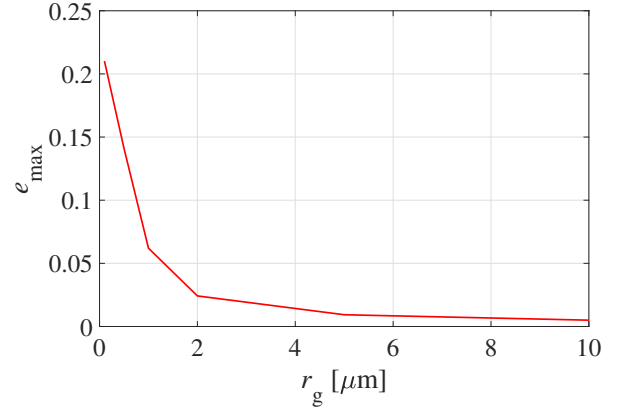


**Figure 4.** Variation in the maximum value of the eccentricity of a particle with initial size of  $10 \mu\text{m}$  as its grain size decreases, which is calculated from the conserved integral of dust particles' motion derived by Hamilton & Krivov (1996).

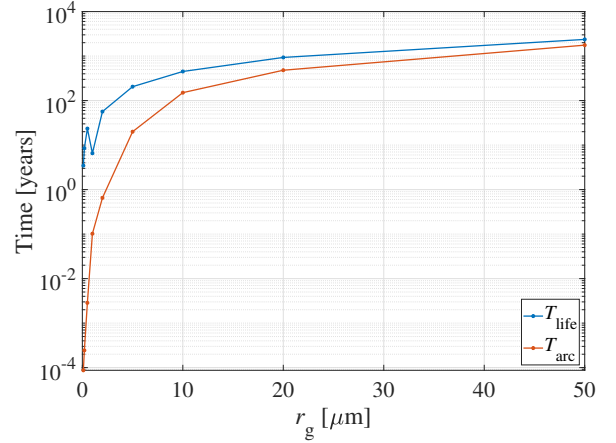


**Figure 5.** Average lifetime  $T_{\text{life}}$  and average time  $T_{\text{arc}}$  that dust particles spend in the arc as a function of grain size.

hit Mimas increases with the grain size. We note that the fraction of particles that hit Aegaeon is very small. This may be attributed to various non-gravitational effects considered in our simulations due to small grain sizes, which makes the distribution of particles dispersed.

## 5 PROPERTIES OF THE G RING

Based on the simulation results of the dynamical evolution of dust particles originating from the G-ring arc, the properties of the simulated ring formed by these particles, including the normal  $I/F$ , the number density of dust particles and the geometric optical depth, can be estimated by integrating the simulated trajectories of dust particles over their size distribution, which reads (Brooks et al. 2004; Liu & Schmidt 2021)

$$4\mu \frac{I}{F}(i_{\text{cell}}, j_{\text{cell}}) = \int_{r_{\text{min}}}^{r_{\text{max}}} \frac{\tilde{n}(i_{\text{cell}}, j_{\text{cell}}, r_g) \pi r_g^2 Q_{\text{sca}}(r_g) P(r_g, \alpha)}{S_{\text{normal}}(i_{\text{cell}}, j_{\text{cell}}) n_{\text{start}}(r_g)} \Delta t N(r_g) dr_g, \quad (3)$$

**Table 1.** Fractions of different final fates of dust particles with different grain sizes. Note that the ‘Move outside’ column represents the fraction of particles that migrate outside the orbit of Enceladus. The fractions of dust particles that hit Enceladus is very small and not listed here.

$r_g(\mu\text{m})$	Removed by sputtering	Hit A ring	Move outside	Hit Mimas	Hit Aegaeon
0.1	0.988	0	0	0	0.012
0.2	1.0	0	0	0	0
0.5	1.0	0	0	0	0
1.0	0	0.955	0	0.023	0.022
2.0	0	0.947	0	0.035	0.018
5.0	0	0.899	0	0.099	0.002
10.0	0	0.473	0.315	0.197	0.003
20.0	0	0.414	0.252	0.33	0.003
50.0	0	0.478	0.148	0.353	0.019

$$\tau(i_{\text{cell}}, k_{\text{cell}}) = \int_{r_{\text{min}}}^{r_{\text{max}}} \frac{\tilde{n}(i_{\text{cell}}, k_{\text{cell}}; r_g) \pi r_g^2}{S_{\text{edge-on}}(i_{\text{cell}}, k_{\text{cell}}) n_{\text{start}}(r_g)} \Delta t N(r_g) dr_g, \quad (4)$$

$$n(i_{\text{cell}}, j_{\text{cell}}, k_{\text{cell}}) = \int_{r_{\text{min}}}^{r_{\text{max}}} \frac{\tilde{n}(i_{\text{cell}}, j_{\text{cell}}, k_{\text{cell}}; r_g)}{V(i_{\text{cell}}, j_{\text{cell}}, k_{\text{cell}}) n_{\text{start}}(r_g)} \Delta t N(r_g) dr_g, \quad (5)$$

where the space around the ring is divided into a series of grid cells indexed by  $(i_{\text{cell}}, j_{\text{cell}}, k_{\text{cell}})$  in the Saturn-centered cylindrical coordinate system. The variable  $\mu_{\frac{I}{F}}(i_{\text{cell}}, j_{\text{cell}})$  denotes the normal  $I/F$  in the region with a surface area of  $S_{\text{normal}}(i_{\text{cell}}, j_{\text{cell}})$  when viewed from above,  $r_{\text{min}}$  and  $r_{\text{max}}$  are the minimum and maximum grain sizes of dust particles in our simulations,  $\tilde{n}(i_{\text{cell}}, j_{\text{cell}}; r_g)$  is the vertically-integrated number of times that dust grains with grain size  $r_g$  pass the region indicated by  $(i_{\text{cell}}, j_{\text{cell}})$ ,  $Q_{\text{sca}}(r_g)$  and  $P(r_g, \alpha)$  are the scattering efficiency and the phase function of dust particles, and both can be calculated by Mie theory (Brooks et al. 2004; Throop et al. 2004),  $n_{\text{start}}(r_g)$  is the number of simulated particles for each grain size,  $\Delta t$  is the constant time-step used for segmenting the trajectories of particles,  $N(r_g)$  is the particle size distribution,  $\tau(i_{\text{cell}}, k_{\text{cell}})$  is the edge-on geometric optical depth of the ring,  $\tilde{n}(i_{\text{cell}}, k_{\text{cell}}; r_g)$  is the number of times that dust particles with grain size  $r_g$  pass the region with a surface area of  $S_{\text{edge-on}}(i_{\text{cell}}, k_{\text{cell}})$  when viewed edge-on,  $n(i_{\text{cell}}, j_{\text{cell}}, k_{\text{cell}})$  is the number density of dust particles in the grid cell with volume  $V(i_{\text{cell}}, j_{\text{cell}}, k_{\text{cell}})$ ,  $\tilde{n}(i_{\text{cell}}, j_{\text{cell}}, k_{\text{cell}}; r_g)$  is the number of times that dust particles with grain size  $r_g$  pass the grid cell  $(i_{\text{cell}}, j_{\text{cell}}, k_{\text{cell}})$ .

The detailed study of the size distribution of dust particles in the G ring shows that the size of dust particles within the G ring can be characterized by a power-law distribution with the exponent  $q$  in the range of [1.5, 3.5] (Throop & Esposito 1998). Results from other studies also support that the size distribution of particles inside the G ring is relatively flat and the value of  $q$  is smaller than 3.5 (Meyer-Vernet et al. 1998; De Pater et al. 2004). Here we assume that the particle size distribution of the ring follows the differential power-law distribution, which is expressed as

$$N(r_g) dr_g = C_0 r_g^{-q} dr_g, \quad (6)$$

where  $C_0$  is the normalization constant. By matching both the normal  $I/F$  estimated from Eq. (3) and the number density estimated from Eq. (5) with that inferred from the observations (Hedman et al. 2007; Ye et al. 2016), we get  $q = 2.8$  and  $C_0 = 4.0$ .

The average radial normal  $I/F$  profiles derived from Eq. (3) are shown in Fig. 6, where the profile in the longitude range of  $[-10^\circ, 10^\circ]$  passes through the arc, and the profile in the longitude

range of  $[170^\circ, 190^\circ]$  passes through elsewhere. One of the fits for deriving the  $q = 2.8$  and  $C_0 = 4.0$  is that aligns the peak value of the simulated normal  $I/F$  in the longitude range of  $[170^\circ, 190^\circ]$  with that of the G ring, which is obtained from the observation (see Hedman et al. 2007, Fig. 2). With  $q = 2.8$  and  $C_0 = 4.0$ , the normal  $I/F$  profiles from our numerical simulations match well with that derived by Hedman et al. (2007), which supports that the G ring may originate from the arc. The radial range of the ring is  $[166, 000, 175, 000]$  km. For the profile through elsewhere, the normal  $I/F$  increases quickly to the peak value of  $3.9 \times 10^{-6}$  at the radial distance of  $\sim 168, 000$  km, and then decreases slowly with the increase of the radial distance from Saturn. For the profile through the arc, the normal  $I/F$  increases and decreases sharply within the radial range of 2, 000 km. Subsequently, the normal  $I/F$  decreases slowly, following the similar trend of the profile through elsewhere. Therefore, most of the arc is confined in the radial range of  $[166, 500, 168, 500]$  km. The peak position of the normal  $I/F$  of the arc is about 167, 500 km, which is close to the 7:6 CER with Mimas (Hedman et al. 2007).

We note that the average normal  $I/F$  in the longitude range of  $[-10^\circ, 10^\circ]$  of our results is slightly higher than that derived by Hedman et al. (2007), the peak values of which are  $2.1 \times 10^{-5}$  and  $1.6 \times 10^{-5}$ , respectively. To analyze the dynamical cause for this difference, we calculate the cumulative distributions of the peak of the normal  $I/F$  of different radial normal  $I/F$  profiles, as shown in Fig. 7. The normal  $I/F$  in the longitude range of  $[-10^\circ, 10^\circ]$  is mainly contributed by dust particles in the range of  $[5, 20] \mu\text{m}$ , followed by the contribution from dust particles larger than  $20 \mu\text{m}$ . For the profile through elsewhere, the contributions of  $[10, 50] \mu\text{m}$  dust particles to the normal  $I/F$  are less than their contributions to the normal  $I/F$  profile through the arc. For these large particles ( $r_g \geq 10 \mu\text{m}$ ), they stay in the arc longer than the small particles (see Fig. 5), and therefore have a higher probability of colliding with the parent bodies in the arc. However, these collisions are not involved in our simulations due to the difficulties of simulating the orbits of a large number of parent bodies. Therefore, we suggest that the slightly higher value of the normal  $I/F$  in the longitude range of  $[-10^\circ, 10^\circ]$  of our results compared to that derived by Hedman et al. (2007) comes from the ignorance of these collisions.

Another fit to get the  $q = 2.8$  and  $C_0 = 4.0$  is that aligns the peak value of the vertical number density at the radial distance of  $2.7 R_s$  with that derived by Ye et al. (2016), as shown in Fig. 8. The red line is the vertical number density profile estimated from Eq. (5), and the black dash line is the fitting result derived from the in-situ measurement by the Cassini spacecraft (Ye et al. 2016). The vertical range of dust particles in both results is about  $[-0.1, 0.1] R_s$ . The position of the peak number density is  $0.005 R_s$  above the equatorial plane in our result, while that derived from the in-situ measurement is close to the equatorial plane. The difference between our result and that derived by Ye et al. (2016) may come from the assumption that the electric potential of dust particles is a constant (see Section. 2). For dust particles smaller than  $0.5 \mu\text{m}$ , which contribute the most to the observed number density (see Fig. 9), this assumption may minimize the variation of the inclination of particles due to the Lorentz force related to the electric potential of particles, which results in the shift of the position of peak vertical number density and the concentrated distribution of dust particles in the vertical direction.

The average radial number density profiles (averaged over the vertical range of  $[-0.1, 0.1] R_s$ ) of dust particles originating from the G-ring arc in different longitude ranges are also derived from Eq. (5), as plotted in Fig. 10. The number density profiles of particles in these two longitude ranges are largely similar, except for the region of the arc with a peak radial number density of about  $0.019 \text{ m}^{-3}$ . In

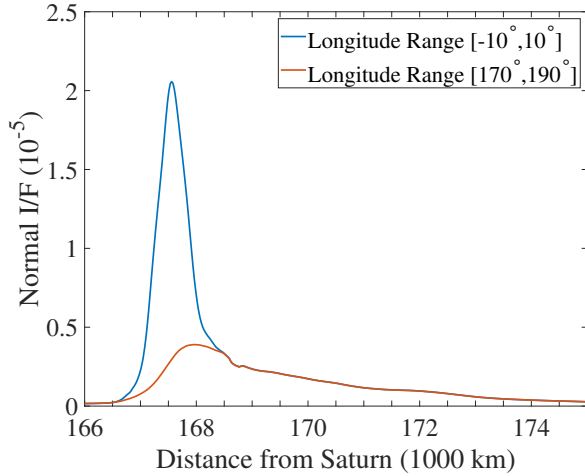


**Figure 6.** Radial profiles of the normal  $I/F$  of the simulated ring formed by dust particles originating from the G-ring arc, which is derived from Eq. (3) with  $q = 2.8$  and  $C_0 = 4.0$ . The profile in the longitude range of  $[-10^\circ, 10^\circ]$  passes through the arc, and the profile in the longitude range of  $[170^\circ, 190^\circ]$  passes through elsewhere. The peak value of the normal  $I/F$  in the longitude range of  $[170^\circ, 190^\circ]$  is aligned with that derived from the observation (see Hedman et al. 2007, Fig. 2).

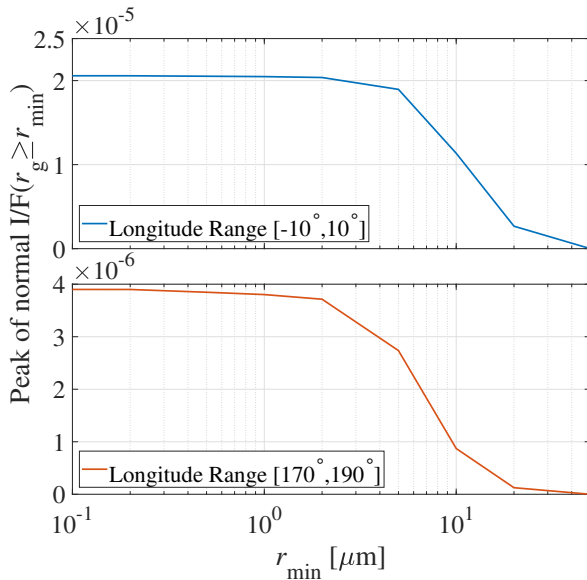


**Figure 7.** Cumulative distributions of the peak of the normal  $I/F$  of different radial normal  $I/F$  profiles of the simulated ring in Fig. 6.

In addition to the G ring, a lot of dust particles originating from the G-ring arc are also distributed in the region between the A ring and the G ring, and there is another peak position of the number density around  $2.67 R_s$ . This peak at  $2.67 R_s$  may be attributed to the fact that particles smaller than  $0.5 \mu\text{m}$  dominate in this region (see Fig. 9), and their number density peaks around this radial distance (see Fig. 11). In the region outside the G ring, the number density is small and decreases to nearly zero outside the orbital distance of Mimas.

The edge-on geometric optical depth of the simulated ring is calculated from Eq. (4). From this result, the apparent edge-on thickness of the G ring which has not been resolved from observations (Nichol-

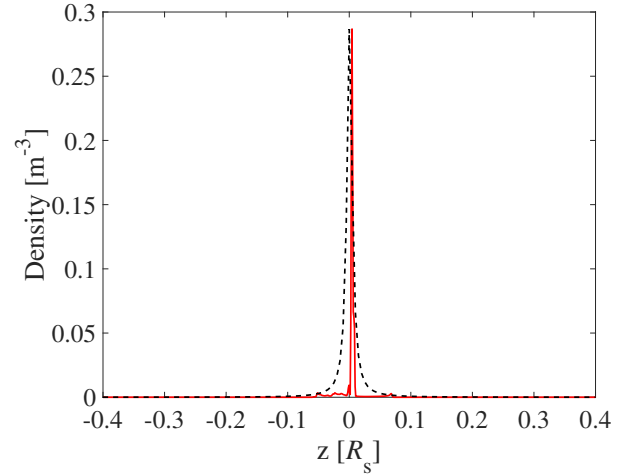


**Figure 8.** Vertical number density profiles at the radial distance of  $2.7 R_s$ . The red line and the black dash line denote the simulated profiles derived from Eq. (5) with  $q = 2.8$  and  $C_0 = 4.0$  and from the in-situ measurement by the Cassini spacecraft (Ye et al. 2016), respectively.

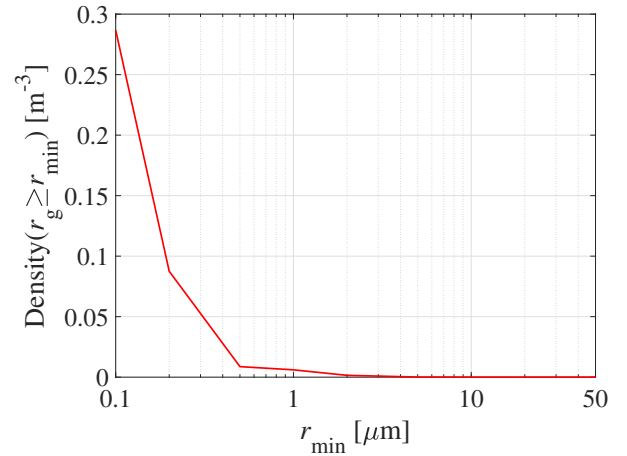


**Figure 9.** Cumulative distribution of the peak vertical number density in Fig. 8.

son et al. 1996) can be constrained (see Fig. 12, where the line of sight passes through the arc). If the observable threshold of the edge-on geometric optical depth of an observing instrument is  $1 \times 10^{-8}$ , the apparent edge-on thicknesses of the inner and outer edges of the G ring are about 9,000 km and 3,000 km, respectively. If the observable threshold is a higher value of  $1 \times 10^{-6}$ , the ring is only observable within a north-south thickness of 650 km, and the vertical range of the ring in the north of Saturn's equatorial plane is tens of kilometers larger than that in the south. In the region of the arc, the edge-on geometric optical depth peaks at a value of  $3.9 \times 10^{-2}$ . Note that when the line of sight does not pass through the arc, the apparent edge-on thickness of the G ring is similar, but the maximum value of the edge-on geometric optical depth is on the smaller order of  $10^{-3}$ .

The mass of dust particles escaping from the arc to the ring per second  $M^+$  can be calculated by integrating the particle size distribution, which reads

$$M^+ = \int_{r_{\min}}^{r_{\max}} \frac{4}{3} \pi r_g^3 \rho_g N(r_g) dr_g. \quad (7)$$

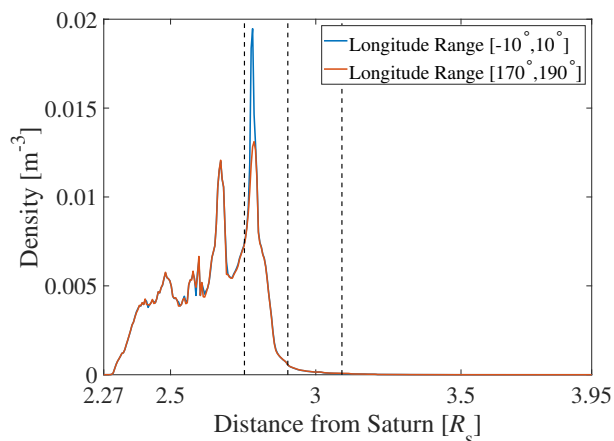


**Figure 10.** Simulated radial number density profiles (averaged over the vertical range of  $[-0.1, 0.1] R_s$ ) of dust particles, where the profile in the longitude range of  $[-10^\circ, 10^\circ]$  passes through the arc, and the profile in the longitude range of  $[170^\circ, 190^\circ]$  passes through elsewhere. The three black dash lines from left to right represent the orbital distances of the inner edge of the G ring ( $166,000 \text{ km} \approx 2.75 R_s$ ), the outer edge of the G ring ( $167,500 \text{ km} \approx 2.78 R_s$ ) and Mimas ( $186,000 \text{ km} \approx 3.09 R_s$ ), respectively.

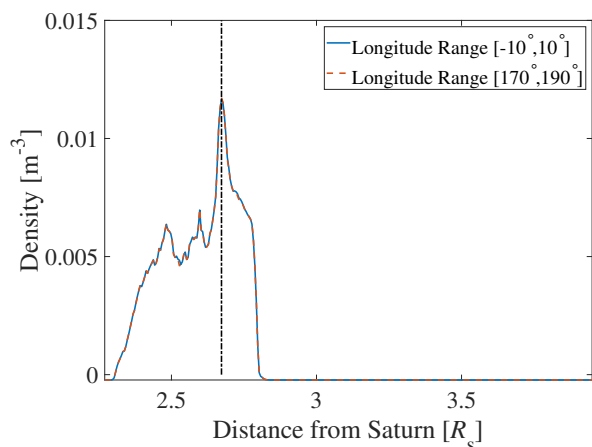


**Figure 11.** Simulated radial number density profiles of particles smaller than  $0.5 \mu\text{m}$  (averaged over the vertical range of  $[-0.1, 0.1] R_s$ ), where the profile in the longitude range of  $[-10^\circ, 10^\circ]$  passes through the arc, and the profile in the longitude range of  $[170^\circ, 190^\circ]$  passes through elsewhere. The black dot-dashed line represents the orbital distance of  $2.67 R_s$ .

By substituting Eq. (6), we get  $M^+ = 5.4 \times 10^{-2} \text{ kg s}^{-1}$ . The mass of the arc has been estimated by Hedman et al. (2007), where the value is  $10^8$ - $10^{10} \text{ kg}$ . Assuming that the  $M^+$  is constant and the G ring is only maintained by the G-ring arc, the upper limit of the remaining lifetime of the ring can be estimated to be on the order of  $10^4$  years by dividing the total mass of the parent bodies by the  $M^+$ . This is a threshold value since the entire mass of arc may not be fully converted to the ring. The mass production rate of dust particles from Aegaeon was estimated by Madeira et al. (2018) and Muñoz-Gutiérrez et al. (2022) to be on the order of  $10^{-7} \text{ kg s}^{-1}$  and  $10^{-5} \text{ kg s}^{-1}$ , respectively, which is much smaller than the  $M^+$ . This suggests that the G ring is dominated by the dust particles from the arc.

In addition, Canup & Esposito (1997) assumed that the G ring

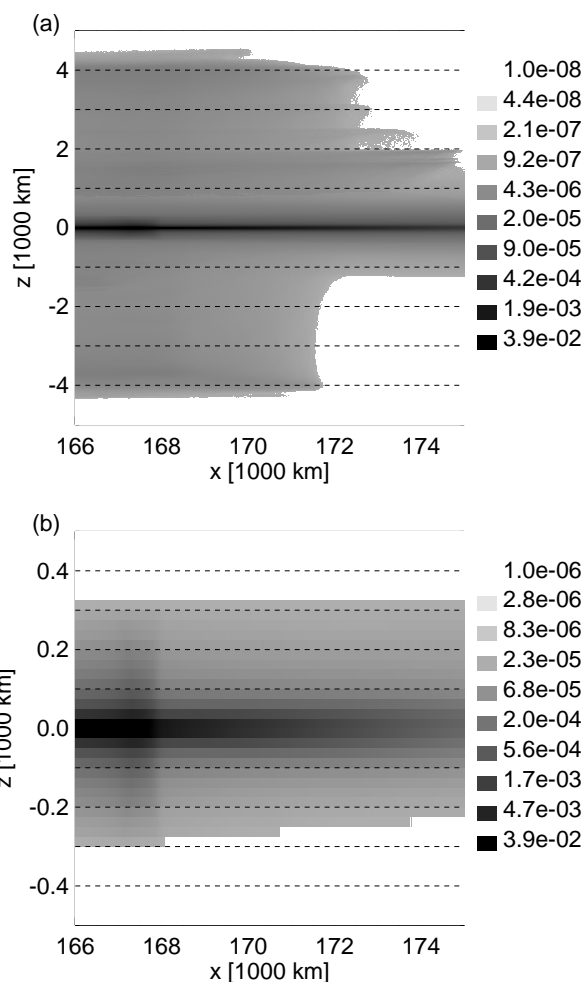


**Figure 12.** Panel a: edge-on geometric optical depth of the simulated ring, where the line of sight passes through the arc; only the values of edge-on geometric optical depth larger than  $1 \times 10^{-8}$  are shown. Panel b: same as Panel a, but only the values of edge-on geometric optical depth larger than  $1 \times 10^{-6}$  are shown.

originates from the breakup of a progenitor satellite, and simulated the time evolution of the number of particles within the G ring. They found that the numerical simulation results with an assumption of a progenitor satellite with a radius of 1.5-3 km match well with the observations. Here we adopt this value to estimate the age of the G ring to be  $10^6$ - $10^7$  years by dividing the total mass of the progenitor satellite by the  $M^+$ .

## 6 CONCLUSIONS

In this paper, the dynamical evolution of particles in the grain size of  $[0.1, 50] \mu\text{m}$  originating from the G-ring arc is studied. Various perturbation forces are considered in the dynamical model, including the effect of planetary oblateness, solar radiation pressure, Poynting-Roberson drag, Lorentz force, plasma drag and the gravity of moons. In addition, the plasma sputtering is also taken into account. We find that particles smaller than  $1 \mu\text{m}$  leave the arc immediately, which are finally removed by the plasma sputtering. The orbital distances of  $1 \mu\text{m}$  particles oscillate with large amplitudes, which leads to the collision between particles and the A ring within a few years. For

particles with  $r_g > 1 \mu\text{m}$ , they stay in the arc for a longer time compared to particles with  $r_g \leq 1 \mu\text{m}$ . These particles can leave the arc due to the plasma sputtering and plasma drag. Generally, dust particles escape from the arc with their grain sizes less than about  $16 \mu\text{m}$ . After leaving the arc, particles move outward due to the plasma drag. Most of these particles finally collide with the A ring, while a small fraction of these particles hit Mimas or Aegaeon. Only particles with  $r_g \geq 10 \mu\text{m}$  have opportunities to move outside the orbital distance of Enceladus.

Based on the study of the dynamics of dust particles, the formation and properties of the G ring are analyzed in this work. By comparing the normal  $I/F$  of the simulated ring formed by particles originating from the G-ring arc and the number density near the G ring to the observations, we get the exponent  $q = 2.8$  for the particle size distribution of the G ring. The good agreement in the normal  $I/F$  between our result and the observation supports that the G ring may originate from the arc. The observed normal  $I/F$  in the part of the ring which passes through the arc is dominantly contributed by  $[5, 20] \mu\text{m}$  particles, while that in other parts of the ring are mainly contributed by  $[5, 10] \mu\text{m}$  particles. The particles detected by the Cassini spacecraft at the radial distance of  $2.7 R_S$  are mainly composed of dust particles smaller than  $0.5 \mu\text{m}$ . The peak value of the average particle number density of the G ring is on the order of  $10^{-2}$ . The region of the arc is the brightest when viewed edge-on, where the value of the edge-on geometric optical depth is  $3.9 \times 10^{-2}$ . If the observable threshold of the edge-on geometric optical depth is  $1 \times 10^{-8}$ , the maximum apparent edge-on thickness of the G ring is about 9,000 km. Based on our result of the particle size distribution of the G ring, the age of the G ring is estimated to be  $10^6$  to  $10^7$  years, and the remaining lifetime of the ring is on the order of  $10^4$  years.

Our results of the properties of the G ring are robust since the relevant perturbation forces are considered and most of the parameters (such as the Saturn gravity field, the solar radiation pressure efficiency and the coefficient of Saturn's magnetic field) used in our dynamical model are known with small uncertainties. The largest uncertainty of our results comes from that we only consider the water group ions  $\text{W}^+$  for the plasma drag in our dynamical model (see Section. 2), while the molecular oxygen ion  $\text{O}_2^+$  also contributes significantly to the plasma in the region of the G ring in the years when Saturn is close to the solstice (Elrod et al. 2012, 2014). This may indicate the G ring also varies seasonally due to the seasonal variation of the plasma in the vicinity of the G ring, which has not been mentioned in previous studies.

## ACKNOWLEDGEMENTS

This work was supported by the National Natural Science Foundation of China (No. 12311530055, 12472048, and 12002397).

## DATA AVAILABILITY

The basic data of this work will be shared on reasonable request to the corresponding author.

## REFERENCES

- Brooks S. M., Esposito L. W., Showalter M. R., Throop H. B., 2004, *Icarus*, 170, 35
- Burns J. A., Lamy P. L., Soter S., 1979, *Icarus*, 40, 1
- Canup R. M., Esposito L. W., 1997, *Icarus*, 126, 28
- Chen Z., Yang K., Liu X., 2024, *Monthly Notices of the Royal Astronomical Society*, 527, 11327
- De Pater I., Martín S. C., Showalter M. R., 2004, *Icarus*, 172, 446
- Dougherty M. K., et al., 2018, *Science*, 362, eaat5434
- Elrod M., Tseng W.-L., Wilson R., Johnson R., 2012, *Journal of Geophysical Research: Space Physics*, 117
- Elrod M. K., Tseng W.-L., Woodson A. K., Johnson R. E., 2014, *Icarus*, 242, 130
- Hamilton D. P., Krivov A. V., 1996, *Icarus*, 123, 503
- Hedman M. M., et al., 2007, *science*, 317, 653
- Hedman M., Cooper N., Murray C., Beurle K., Evans M., Tiscareno M., Burns J., 2010, *Icarus*, 207, 433
- Jacobson R. A., 2022, *The Astronomical Journal*, 164, 199
- Johnson R., Famá M., Liu M., Baragiola R., Sittler Jr E., Smith H., 2008, *Planetary and Space Science*, 56, 1238
- Juhász A., Horányi M., 2002, *Journal of Geophysical Research: Space Physics*, 107, SMP 1
- Jurac S., Johnson R., Richardson J., 2001, *Icarus*, 149, 384
- Lissauer J. J., French R. G., 2000, *Icarus*, 146, 12
- Liu X., Schmidt J., 2018, *Astronomy & Astrophysics*, 609, A57
- Liu X., Schmidt J., 2021, *Monthly Notices of the Royal Astronomical Society*, 500, 2979
- Liu X., Sachse M., Spahn F., Schmidt J., 2016, *Journal of Geophysical Research: Planets*, 121, 1141
- Madeira G., Giuliatti Winter S. M., 2020, *The European Physical Journal Special Topics*, 229, 1527
- Madeira G., Sfair R., Mourão D., Giuliatti Winter S., 2018, *Monthly Notices of the Royal Astronomical Society*, 475, 5474
- Maravilla D., Leal-Herrera J., 2014, *Revista mexicana de astronomía y astrofísica*, 50, 341
- Meyer-Vernet N., Lecacheux A., Pedersen B. M., 1998, *Icarus*, 132, 311
- Muñoz-Gutiérrez M. A., Granados Contreras A. P., Madeira G., A'Hearn J. A., Giuliatti Winter S., 2022, *Monthly Notices of the Royal Astronomical Society*, 511, 4202
- Nicholson P. D., et al., 1996, *Science*, 272, 509
- Persoon A., et al., 2020, *Journal of Geophysical Research: Space Physics*, 125, e2019JA027545
- Showalter M. R., Cuzzi J. N., 1993, *Icarus*, 103, 124
- Smith B. A., et al., 1981, *Science*, 212, 163
- Sun K.-L., Seiß M., Hedman M., Spahn F., 2017, *Icarus*, 284, 206
- Thomas P., Burns J., Hedman M., Helfenstein P., Morrison S., Tiscareno M., Veverka J., 2013, *Icarus*, 226, 999
- Throop H. B., Esposito L. W., 1998, *Icarus*, 131, 152
- Throop H., Porco C., West R., Burns J., Showalter M., Nicholson P., 2004, *Icarus*, 172, 59
- Tseng W.-L., Johnson R., Elrod M., 2013, *Planetary and Space Science*, 77, 126
- Van Allen J. A., 1983, *Journal of Geophysical Research: Space Physics*, 88, 6911
- Wahlund J.-E., et al., 2005, *Geophysical research letters*, 32
- Yang K., Schmidt J., Feng W., Liu X., 2022, *Astronomy & Astrophysics*, 659, A120
- Ye S.-Y., Gurnett D. A., Kurth W. S., 2016, *Icarus*, 279, 51

This paper has been typeset from a  $\text{\TeX}/\text{\LaTeX}$  file prepared by the author.